Reproducing and Attributing IASI Radiance Trends with EC-Earth Climate Model Simulations

Reproducing and Attributing IASI Radiance Trends with EC-Earth Climate Model Simulations

Stefano Della Fera [a], Federico Fabiano [b], Piera Raspollini [a], Marco Ridolfi [c], Jost von Hardenberg [d], Ugo Cortesi[a]

[a] Institute of Applied Physics, National Research Council (IFAC-CNR), Sesto Fiorentino (FI), Italy

[b] Institute of Atmospheric Sciences and Climate, National Research Council (ISAC-CNR), Bologna (BO), Italy

[c] National Institute of Optics, National Research Council (INO-CNR), Sesto Fiorentino (FI), Italy

[d] Department of Environment, Land and Infrastructure Engineering, Politecnico di Torino, Torino (TO), Italy

Corresponding author: Stefano Della Fera, s.dellafera@ifac.cnr.it

ABSTRACT: The evolution of spectrally resolved outgoing longwave radiation measured at the top of the atmosphere (TOA) reflects the fingerprints of key geophysical variables, serving as a powerful tool for studying climate change. In this work, trends in TOA brightness temperature (BT) in the mid-infrared spectral range observed by the Infrared Atmospheric Sounding Interferometer (IASI) are compared with trends in synthetic BTs generated from a set of atmosphere-only simulations with the EC-Earth3 climate model (v3.3.3), over the period 2008-2019. Despite the presence of spectral biases, the model simulations effectively reproduce the IASI trends in the thermal infrared. A spectral kernel analysis is then applied to the synthetic radiances to quantify the contributions of temperature, surface temperature, water vapor, clouds, and greenhouse gases to these trends. The negative trend found in the core of the CO_2 band is attributed to the stratospheric cooling, which is overestimated in the climate model simulations. In the wing of the CO_2 band, the negative trend in radiance results from the combined effect of a positive contribution from the increasing tropospheric temperature and a negative contribution driven by rising atmospheric CO_2 concentration. In the atmospheric windows, clouds have a negative impact on the radiance trend and also significantly affect the inter-annual variability of the model's radiance. Lastly, the near-zero trend in the water vapor band reflects a balance between the positive trend driven by temperature increases and the negative trend associated with water vapor changes. This work highlights the utility of spectrally resolved radiances to disentangle forcing and feedback processes, improving climate model evaluation.

1. Introduction

The present-day evolution of the Earth's climate is primarily driven by the anthropogenically modified concentrations of greenhouse gases (GHGs) and aerosols in the atmosphere, which alter the planet's radiative equilibrium, triggering various feedback mechanisms.

In the linear feedback approximation (Gregory et al. 2004), the Earth's energy imbalance (EEI) at the top of the atmosphere (TOA) - defined as the difference between absorbed solar radiation (ASR) and the outgoing longwave radiation (OLR) - is expressed in terms of an external radiative forcing F and the net climate feedback as:

$$EEI = \Delta F + \lambda \Delta T_s \tag{1}$$

where ΔF presents the effective radiative forcing, i.e., the change in net energy at TOA caused by an external or internal perturbation; λ, the net feedback parameter, contains all the processes resulting as a response to variations in surface temperature ΔT_s.

Over time scales much longer than those affected by internal variability, the EEI at TOA should tend to zero (i.e., the feedbacks completely compensate the forcings):

$$\Delta F = -\lambda \Delta T_s \tag{2}$$

However, in recent decades, the sharp increase in GHGs concentration, which drives the increase in ΔF, has exceeded the planet's radiative response ($\lambda \Delta T_s$), leading to a rapid rise in the EEI and pushing the climate system further from equilibrium (Raghuraman et al. 2021). A comprehensive study by von Schuckmann et al. (2020) estimated that, over the period 1971–2018, the planet's energy imbalance was 0.47 ± 0.10 Wm^{-2}. More recently, for the years 2010–2018, this estimate rose to 0.87 ± 0.12 Wm^{-2}. Notably, nearly all this surplus of energy (about 93 %) remains trapped in the ocean in the form of heat (Meyssignac et al. 2019).

The OLR (Wm^{-2}) represents the infrared energy flux emitted by the planet and plays a pivotal role in regulating its cooling. It is highly sensitive to GHGs concentrations and other key climate-controlling variables. For this reason, long-term OLR measurements from space have become fundamental for climate studies and for assessing the performance of global climate models (GCMs) (Wild 2020). The first mission aimed at measuring and monitoring the planet's longwave, shortwave

and total energy fluxes was the Earth Radiation Budget Experiment (ERBE) (Barkstrom 1984) started in the mid-1980s. Since the early 2000s, the Geostationary Earth Radiation Budget (GERB) mission performed measurements of the Earth Radiation Budget (ERB) alongside the energy fluxes provided by the Cloud and Earth Radiant Energy System (CERES) (Wielicki et al. 1996; Loeb et al. 2018). CERES is currently regarded as the standard benchmark for tuning global climate models (Hourdin et al. 2017). Raghuraman et al. (2021) show that the trend of CERES OLR is 0.28 ± 0.22 W m^{-2} decade^{-1} over the period 2001-2020, resulting from the combined effect of a positive contribution of the feedbacks to the OLR trend (energy release of the system) and a negative contribution of the forcings to the OLR trend (energy trapping within the system). In this context, Loeb et al. (2022) highlighted the substantial regional differences in OLR between CERES observations and the ECMWF Reanalysis v5 (ERA5).

Adding to CERES' integrated fluxes, we can also rely on spectrally resolved radiance measurements ($\mathrm{Wm^{-2}(cm^{-1})^{-1}sr^{-1}}$) in the mid-infrared region of the Earth emission spectrum, ranging from approximately 650 to 2500 cm^{-1} (4 - 15 μm), provided by instruments such as the Atmospheric Infrared Sounder (AIRS, 2002-present, Aumann and Miller 1995), the Infrared Atmospheric Sounding Interferometer (IASI, 2006-present, Hilton et al. 2012) and the Cross-track Infrared Sounder (CrIS, 2011-present, Bloom 2001). IASI Next-Generation (IASI-NG), scheduled for launch in 2025, will continue monitoring the mid-infrared range of the spectrum in the near future (Crevoisier et al. 2014). Moreover, the Polar Radiant Energy in the Far-InfraRed Experiment (PREFIRE, from 2024) (Padmanabhan et al. 2019) and the FORUM (Far-Infrared Outgoing Radiation and Monitoring, from 2027) mission (Palchetti et al. 2020), will offer unique spectrally resolved measurements of the far-infrared (FIR) spectral range, from 100 to 667 cm^{-1} (15 - 100 μm). These missions will address the current observational gap in Earth's emission spectrum from space.

Despite their potentiality, spectral measurements are still under-exploited for the study of the EEI and the assessment of climate forcing and feedbacks. Furthermore, while integrated fluxes are commonly used to tune climate models and evaluate their accuracy in representing the ERB, they can obscure compensating spectral errors within the models, as noted by Huang et al. (2006) and Huang et al. (2007). For instance, Della Fera et al. (2023) found that although the integrated fluxes from the EC-Earth3 GCM showed good agreement with CERES broadband fluxes, a comparison

of spectral radiances with IASI revealed several biases in the model, some of which were opposite in sign.

The causes of biases in spectrally resolved OLR ($\mathrm{Wm}^{-2}(\mathrm{cm}^{-1})^{-1}$) can be identified more readily compared to biases in broadband OLR, as spectrally resolved quantities carry distinct signatures of key climate variables, including temperature, water vapor, gas concentrations, and clouds. For this reason, the spectral dimension of climate feedbacks plays a pivotal role in understanding the processes shaping the climate system and constraining climate models.

In this perspective, Raghuraman et al. (2023) analyzed the spectrally resolved OLR trends derived from AIRS data (2003–2021) and the experiments conducted with the Geophysical Fluid Dynamics Laboratory GCM, quantifying the impact of GHGs on spectral radiation by disentangling the forcing and feedback components in the OLR. Along the same line, Roemer et al. (2023) demonstrated the feasibility of utilizing IASI satellite observations (2007-2020) to directly infer spectral climate feedbacks from inter-annual and seasonal variability.

Whitburn et al. (2021) analyzed the spectrally resolved OLR trends of IASI clear-sky measurements over the period 2008-2017, identifying key indicators of recent climate change. In the same context, Huang et al. (2022) used 17 years of AIRS-observed radiances and simulated radiances to estimate spectral trends in clear-sky conditions and to isolate the contributions of individual variables to these trends. Also using AIRS data, Pan et al. (2015) analyzed the evolution of stratospheric temperatures through spectral kernel analysis (Huang et al. 2014). Furthermore, by incorporating data from Advanced Microwave Sounding Unit A (AMSU-A) and climate model simulations, Pan et al. (2017) distinguished between the impacts of natural variability and external forcings on stratospheric temperatures.

In line with previous studies, we analyze trends in IASI spectrally resolved radiances under all-sky conditions for the period 2008 to 2019 and compare them to trends in synthetic radiances generated by a IASI simulator implemented in the EC-Earth global climate model. The primary goal of this analysis is to assess whether the trends in spectral radiances observed over this relatively short period are statistically significant, and to evaluate the ability of a single climate model to accurately reproduce these trends. By doing so, the study demonstrates how the combined use of climate models and observations can provide a robust assessment of model performance, while also offering insights into recent climate evolution on decadal timescales.

In addition to comparing simulated and observed trends, we apply a spectral kernel analysis (Soden et al. 2008; Huang et al. 2014) to the trends in synthetic radiances to attribute them to individual climate variables. This approach also enables us to distinguish between stratospheric and tropospheric contributions, which exhibit distinct behaviours in their influence on the OLR trend. Moreover, the analysis allows us to separate between external forcing, driven by the impact of GHGs on radiation, and the feedback mechanisms characterizing the climate system's response.

The structure of the paper is as follows: Section 2 describes the observed and synthetic datasets utilized in this study and provides an overview of the updated version of the IASI simulator employed for the climate model simulations. The results are presented in Sections 3 and 4. Section 3 focuses on the comparison of trends in simulated and observed radiances, while Section 4 attributes the origin of these trends through a decomposition of the radiances using a kernel analysis. Finally, a discussion and the conclusions are provided.

2. Data and Methods

a. IASI all sky radiances over the period 2008 - 2019

IASI is a Fourier Transform Spectrometer developed at the Centre national d'études spatiales (CNES) in cooperation with the European Organisation for the Exploitation of Meteorological Satellites (EUMETSAT). It was launched in October 2006 onboard the MetOp-A (Meteorological Operational Satellites) satellite and it was followed by two other identical instruments (IASI-B and IASI-C) onboard MetOp-B (launched in 2012) and MetOp-C (launched in 2019) (Edwards and Pawlak 2000). All the three IASI instruments provide measurements of spectrally resolved radiances covering the spectral range from 645 to 2760 cm^{-1}, commonly known as the mid-infrared range. This range encompasses absorption lines of a wide set of atmospheric gases, including CO_2, CH_4, O_3, N_2O, CO, SO_2, NH_3, CFC-11, CFC-12, and others (Harries et al. 2008).

The IASI instruments sample the spectrum with a step of 0.25 cm^{-1}, providing data across 8461 channels. The spectral resolution is of 0.5 cm^{-1}. The MetOp satellites follow a sun-synchronous polar orbit with the equatorial crossing time of the ascending node at 9:30 AM (local time) and descending node of the orbit at 9:30 PM (local time). The satellite repeat cycle is of 29 days but IASI measurements achieve the global Earth coverage every 2 days because the instrument's line of sight is scanned in the across-track direction, with a swath of ±48° on either side of the orbit

track. Each across-track swath is composed of 30 field of regards (FORs), each of them containing 4 Field of Views (FOVs) with a ground pixel diameter of about 12 km.

In this work, we collected 12 years of IASI (MetOp-A) data for the period 2008 - 2019. Data from 2008 to 2016, taken from the Fundamental Climate Data Record (FCDR) of reprocessed Metop-A Level 1c product (EUMETSAT 2018), are extended with operational data of the same instrument until the 2019. All these IASI data were provided by the European Weather Cloud (EWC) service.

To build the all-sky IASI climatology, we followed the approach outlined in Della Fera et al. (2023). While in that study only daytime measurements were used, here we include both daytime and nighttime near-nadir spectra. i.e., for each swath, we considered only the spectra corresponding to the 8 ground pixels closest to the satellite ground track. To mitigate any bias that may arise from an un-even sampling of the measurements of a given area during day- and night- times, we first averaged the daytime and nighttime measurements separately, then combining the two averages with equal weights to get a monthly average. Finally, to limit the spatial mismatch between observations and simulations, IASI spectra were averaged into 2°x2° cells centered on the gridboxes of the climate model where the synthetic measurements are actually simulated.

b. Synthetic IASI radiances from the EC-Earth3 climate model

The EC-Earth3 climate model (v 3.3.3), in the rest of the paper referred as EC-Earth3, is a state-of-the-art Earth-system model developed by a European consortium, which participated in the last intercomparison project (CMIP6, (Eyring et al. 2016)). The atmospheric component of the climate model is represented by the Integrated Forecast System (IFS cy36r4) of the European Centre for Medium-Range Weather Forecasts (ECMWF) (Haarsma et al. 2020), while the oceanic component is represented by NEMO 3.6 (Madec 2015). For the other components of the model (sea ice, land, etc.) and more detailed information about the model structure, we refer to Döscher et al. (2021). Similar to other CMIP6 models, EC-Earth3 has been tuned on the basis of the observed CERES fluxes (Wild 2020; Döscher et al. 2021).

1) Update of the IASI simulator inside EC-Earth3: extension to all-sky conditions

Della Fera et al. (2023) implemented in EC-Earth3 a IASI simulator based on the $\sigma - IASI$ radiative transfer model (Amato et al. 2002; Serio et al. 2023; Masiello et al. 2022, 2024). In that work, the radiative transfer model was integrated in the COSP (v1.4.1) module (Bodas-Salcedo et al. 2011) in order to perform online calculations of the clear-sky spectrally resolved radiances starting from the instantaneous climate model fields. Specifically, prognostic variables from the model (such as pressure, surface emissivity and temperature, air temperature, water vapor, and ozone) are directly supplied to $\sigma - IASI$ through COSP. Additionally, GHGs concentrations for carbon dioxide, methane, and nitrous oxide are sourced from the standard forcing dataset used for historical CMIP6 runs (Meinshausen et al. 2020). The vertical concentration profiles of the other trace gases required by $\sigma - IASI$ (SO_2, HNO_3, NH_3, OCS, HDO, and CF_4) are kept fixed and are taken from the U.S. Standard Atmosphere of the Atmospheric Constituent Profiles dataset (Anderson et al. 1986), as they are not included in this version of EC-Earth3.

In this work, the IASI simulator has been extended to operate under all-sky conditions. While cloud cover and the profiles of cloud ice and liquid water content are prognostic variables provided by the IFS model within EC-Earth3, the effective radii of cloud particles are parameterized following the schemes of Martin et al. (1994) and Ou and Liou (1995). These variables—cloud cover, cloud ice and liquid water content profiles, and the effective radii of ice crystals and water droplets—are then passed to the radiative transfer model to simulate TOA radiances under cloudy conditions. In σ-IASI, the treatment of cloud multiple scattering follows the parameterization described by Chou et al. (1999).

When comparing observed and simulated radiances, the most critical aspect lies in the choice of an accurate approach to account for the cloud distribution across the very different spatial scales represented by the EC-Earth3 gridbox (an area of approximately 6000 km^2) and the IASI FOV (an area of about 100 km^2). This issue is also crucial within the built-in radiative scheme of the climate model, since assuming homogeneous cloud fields inside the large EC-Earth3 gridbox results in a poor approximation. In order to simulate the sub-grid cloud variability, some assumptions are made on how clouds are distributed horizontally and vertically, and how clouds at different altitudes overlap. For instance, the Rapid Radiative Transfer Model (RRTM, (Mlawer et al. 1997)) integrated in EC-Earth3 computes OLR in a limited number of sub-intervals of the spectrum handling the

subgrid-scale cloud variability by generating a set of subcolumns based on an overalap assumption to which the Monte Carlo Independent Column Approximation (MCICA) algorithm (Pincus et al. 2003) is applied. Therefore, rather than computing the total flux F_{tot} as the average of fluxes calculated for each subcolumn F_n:

$$F_{tot} = \frac{1}{N} \sum_{n=1}^{N} F_n \tag{3}$$

McICA uses stochastic sampling to efficiently estimate the impact of subgrid cloud variability on radiative fluxes

$$F_{McICA} \approx \sum_{k=1}^{K} F_{n_k,k} \tag{4}$$

where $F_{n_k,k}$ is the monochromatic flux computed in K spectral intervals for a single randomly selected sub-column n_k.

The most common assumption, also used in EC-Earth3, is the maximum-random overlap, though more accurate assumptions can be derived from observations (Hogan and Illingworth 2000). The subcolumns are stochastically generated using the maximum-random overlap assumption and are identified by binary values (0 clear, 1 cloudy) at each layer. Then, the vertical profiles of liquid and water cloud content in the gridbox are multiplied by the binary profile for each subcolumn. The overall set of subcolumn profiles is generated based on a random probability distribution function, with the constraint that its integral equals the average gridbox value. In this work, we follow the same approach integrated in the RRTM model by exploiting the Subgrid Cloud Overlap Profile Sampler (SCOPS) (Räisänen et al. 2004), already contained in the COSP package present in the EC-Earth3 model. More in detail, we provide the cloud fraction of the EC-Earth3 model at each of the 91 IFS layers to SCOPS, which produces a fixed number of subcolumns for each gridbox. SCOPS can provide an arbitrary number of subcolumns on the basis of three overlap assumptions: maximum, random and maximum-random. We selected the maximum-random overlap assumption and 50 sub-columns. This number of sub-columns ensures that the size of a sub-column is comparable to the size of the IASI instrument's FOV. Then, the online radiative transfer computation is performed by $\sigma - IASI$ on the basis of the subcolumns profiles and not

using the mean gridbox profile information. To replicate an IASI measurement, a single subcolumn is randomly selected from each model grid box at each time step. In this way, we adopt an approach analogous to the McICA approximation. Instead of computing the temporal average of the radiance R_{tot} by considering radiances from all subcolumns in a model grid cell:

$$R_{tot} = \frac{1}{N}\frac{1}{T}\sum_{n=1}^{N}\sum_{t=1}^{T} R_{n,t} \tag{5}$$

where $R_{n,t}$ is the radiance computed for the n-th subcolumn at each time step t of the time range T, we randomly pick only one subcolumn n in each grid cell for each time step t:

$$R_{tot} \approx \frac{1}{T}\sum_{t=1}^{T} R_{n_t} \tag{6}$$

Here R_{n_t} is the radiance computed at time step t for a randomly selected subcolumn n. This approach significantly mitigates the prohibitive computational costs associated with simulating radiances for all the 50 subcolumns generated per grid box.

2) Output of the IASI simulator

The Earth's emission spectrum is simulated at nadir-view by the $\sigma - IASI$ integrated in the EC-Earth3 model from 100 to 2600 cm^{-1}. However, the analysis conducted in Section 3 focuses specifically on the MIR range, which is the range measured by IASI, and it is limited to 2250 cm^{-1}, to avoid contamination from solar radiation. The indicative ranges of the main absorption bands are presented in Table 1. In order to reduce the data storage, the high-resolution output of $\sigma - IASI$ is convolved with a 10 cm^{-1} wide box function. We also convolve the high-resolution radiances with the IASI instrumental response function (a Gaussian with a Full Width at Half Maximum of 0.5 cm^{-1}) to get the simulated radiance at 14 spectral channels (listed in Table 2), specifically chosen for their relevance in capturing the evolution of some key climate variables. The selection of these high-resolution channels is based on the analysis of the weighting functions, defined as the derivatives of the transmittance of an atmospheric layer extending from a given height to the TOA, with respect to the bottom height of the layer itself. This method ensures that channels are

selected from various absorption bands, providing sensitivity to key climate variables at different atmospheric layers.

Weighting functions are computed for both clear- and cloudy-sky conditions using the climatological profiles of the U.S. standard atmosphere of the Atmospheric Constituent Profiles dataset (Anderson et al. 1986).

Acronym	Band Details	Spectral Range (cm^{-1})
CO_2	Carbon Dioxide	650 - 750
AW1	Atmospheric Window (1)	800 - 950
O_3	Ozone	980 - 1080
AW2	Atmospheric Window (2)	1100 - 1250
CH_4	Methane	1200 - 1400
N_2O	Nitrous Oxide	1250 - 1350
WV	Water vapor	1200 - 1850

TABLE 1. Spectral intervals of the atmospheric windows and of the main absorption bands highlighted in Fig. 1.

The first column of Table 2 shows the wavenumbers of the selected channels; the second column indicates the main variables influencing radiances at TOA at that wavenumber and the third column shows the altitude range where the weighting function peaks (in clear-sky conditions). It is worth noting that clouds affect the computation of the transmittance and weighting functions, so the altitudes listed in Table 2 are only indicative, particularly in spectral ranges where the radiance is heavily influenced by clouds (e.g., atmospheric windows, water vapor bands). The 14 selected channels are also highlighted in Figure 1, which shows a simulated Earth emission spectrum over the MIR spectral range, generated using the U.S. Standard Atmosphere from the Atmospheric Constituent Profiles dataset (Anderson et al. 1986), with the main absorption bands highlighted (see also Table 1).

3) CONFIGURATION OF THE CLIMATE MODEL SIMULATIONS

We conduct three atmosphere-only historical simulations for the period 2008-2019, each with different initial conditions, with the IASI simulator activated. The sea surface temperature (SST) and sea ice concentration (SIC) are constrained by observations following the Atmospheric Model Intercomparison Project (AMIP) protocol configuration for CMIP6. The horizontal resolution of the EC-Earth3 climate model grid is about 80 km (TL255L91-ORCA1) but, to save some computing

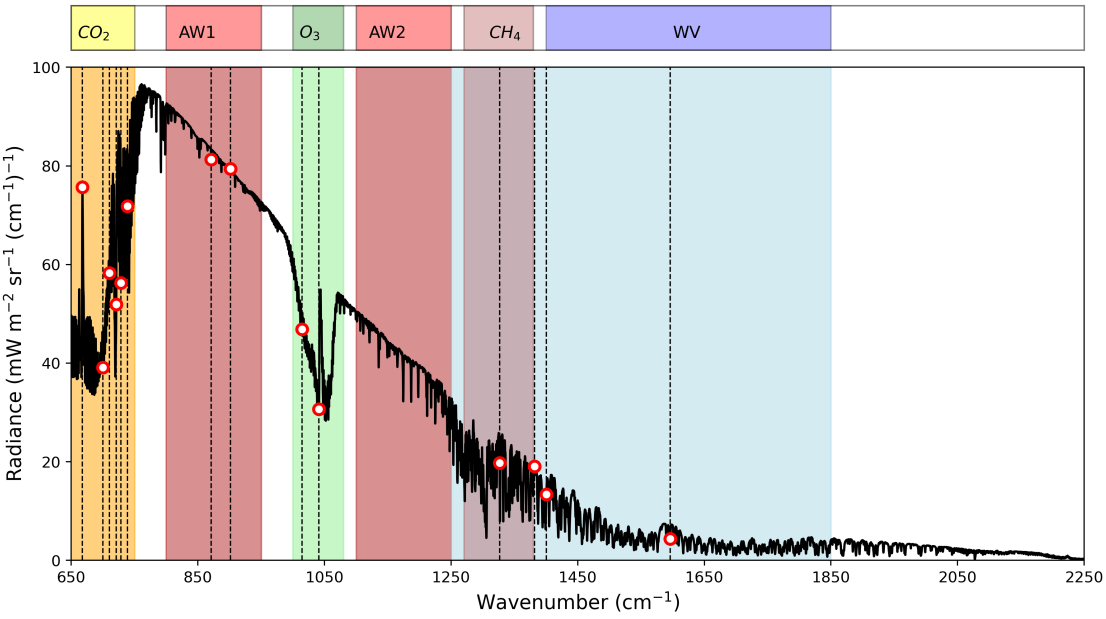

FIG. 1. Simulated spectrum with red points marking the selected channels listed in Table 2. The key spectral bands of Table 1 are highlighted with different colors and labeled at the top of the figure. Note that the shaded area representing the water vapor band overlaps with that of CH_4. Additionally, the N_2O spectral band is not shown, as it is entirely overlapped by the CH_4 absorption band.

time, the IASI spectra are simulated every four latitude and every four longitude grid points of the model, as in the clear-sky case (Della Fera et al. 2023). Unlike in the clear-sky analysis of Della Fera et al. 2023, here, the temporal resolution of the climate model output spectra is increased from 6 hours to 3 hours. This adjustment was made to better capture cloud variability and, consequently, improve the representation of the interaction of clouds with the infrared radiation. The cost of the simulations is significantly higher compared to clear-sky conditions. The overall computational cost of the all-sky climate model simulations increases from approximately 4000 core hours per simulated year (CHPSY) for the clear-sky case to around 9000 CHPSY, 18 times more expensive than a standard simulation without the IASI simulator (about 500 CHPSY).

3. Mean state and trends in observed and simulated radiances

Here, we present the results of the comparison between the radiance trends observed by IASI and those obtained with EC-Earth3 and the IASI simulator. The analysis has been conducted using

Channel (cm^{-1})	Variables	Altitude
667.75	T, CO_2	middle stratosphere
700.25	T, CO_2	lower stratosphere and upper troposphere
710.25	T, CO_2	upper troposphere and lower stratosphere
721.25	T, CO_2	middle troposphere
728.50	T, CO_2	low troposphere
739.00	T, CO_2	low troposphere
871.25	T, H_2O	surface and low troposphere
901.50	T, H_2O	surface and low troposphere
1014.50	T, O_3	stratosphere and troposphere
1041.00	T, O_3	stratosphere and troposphere
1326.75	T, H_2O	low troposphere
1381.75	T, H_2O	middle troposphere
1400.50	T, H_2O, CH_4, N_2O	middle troposphere
1596.25	T, H_2O	upper troposphere

TABLE 2. High-resolution channels selected for the analysis. The first column shows the wavenumbers of the channels. The second column identifies the variables influencing the radiance in each channel, while the third column indicates the atmospheric layers to which the channel is most sensitive.

the spectral radiances, or, alternatively, the Brightness Temperature (BT), i.e. the temperature a black body should have to emit that specific radiance.

To have an overview of the model spectral biases, we first compare the time-average of observed and simulated radiances over the entire period in latitude and spectral bins (Subsection 1). We then present the procedure used to compute the radiance trends (Subsection 2) and finally, in Subsection 3, we show and discuss the results of the comparison.

Note that, to avoid the still large uncertainties existing on the land surface emissivity models, the analyses are limited to geographical areas over the ocean. The comparison strategy adopted to assess synthetic versus observed spectral radiances may not be appropriate over land, where spatial and temporal mismatches can introduce significant biases, particularly in channels sensitive to the surface and lower atmosphere (Whitburn et al. 2021).

1) Mean state biases

Figure 2 shows the differences between the synthetic BTs generated with EC-Earth3 + IASI simulator and the observed BTs from IASI measurements, with a spectral sampling of 10 cm^{-1} for latitudes between 60°N and 60°S (ocean only). The top panel, adapted from Figure 3 of Della Fera et al. (2023), shows the BT differences between EC-Earth3 and IASI in clear-sky conditions, while the bottom panel refers to all-sky conditions (using the set of simulations and observations described above). This comparison is limited to the period 2008-2016, for which both sets of clear- and all-sky EC-Earth3 simulations (clear and cloudy) are available.

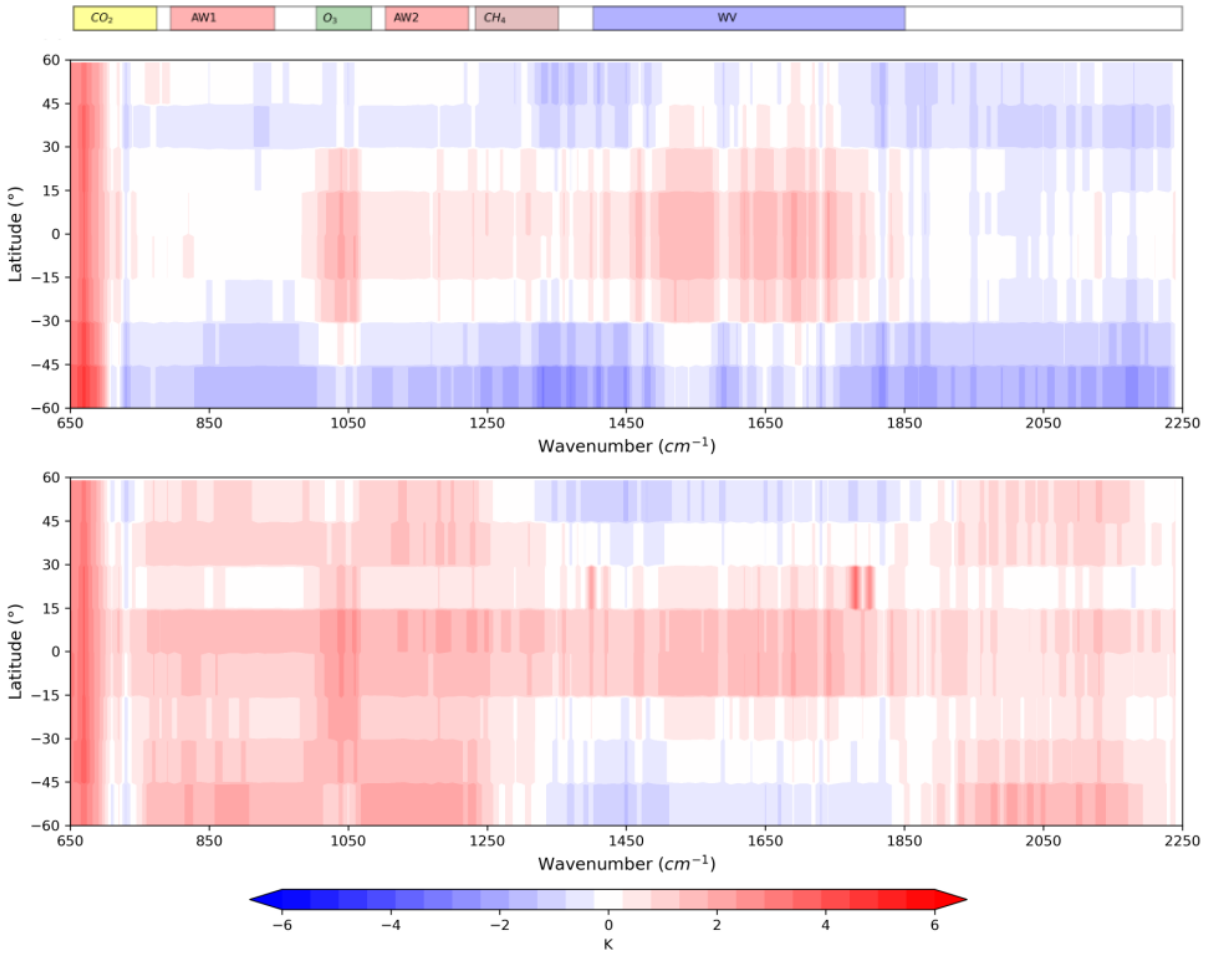

Fig. 2. Brightness temperature (BT) differences (model–observations) over ocean, in clear sky conditions (top panel) and in all-sky conditions (bottom panel) over the period 2008–2016. The top panel is an adaptation from Fig. 3 of Della Fera et al. (2023).

The biases present in the CO_2 band [650-750 cm^{-1}] are nearly identical in clear-sky and all-sky conditions. Since the CO_2 concentration is prescribed by observations in the model simulations, the biases in this spectral range can be primarily attributed to temperature biases in the model. In the core of the band [650 – 690 cm^{-1}], CO_2 molecules show their maximum absorption and, as a consequence, the atmosphere is almost completely opaque. Consequently, the radiation measured in this spectral region is primarily emitted from the stratosphere and upper troposphere, making it generally unaffected by the presence of clouds. The difference between EC-Earth3 and IASI BTs reaches a peak of about 3.5 K in the core of the CO_2 band and gradually decreases towards the band's wing, which is sensitive to different altitudes from upper to lower troposphere. The stratospheric warm bias in the IFS model is well documented, and various improvements to the model physics have been successfully tested since cycle 36 (the IFS version inside EC-Earth3), including enhancements in ozone representation, radiative transfer approximations, and a more accurate representation of the solar spectrum (Hogan et al. 2017).

The most evident difference between the two panels in Figure 2 appears in the atmospheric windows (AW1, AW2), regions that are extremely sensitive to surface temperature and to the temperature and water vapor of the first atmospheric layers. In clear-sky conditions the bias is close to zero, in particular in the tropics and subtropics, because the model SST are prescribed by observations. In all-sky conditions, however, a consistent bias of approximately 1 K is observed across all latitudes, with a more pronounced effect in the tropics. This bias is most likely attributable to the representation of clouds in the model. Indeed, it is important to note that, in the presence of clouds, the radiation emitted at altitudes below the clouds does not reach the TOA, making the atmospheric windows highly sensitive to the cloud distribution and, if the clouds are particularly thick, to the temperature of cloud tops.

The positive bias of the EC-Earth3 BT in the AW1 and AW2 agrees with what Lacagnina and Selten (2014) obtained in their work regarding cloud biases in the model. Their analysis showed that EC-Earth (version 2.3) generally underestimates cloud cover across all latitudes, while overestimating cloud optical thickness. This combination leads to an overestimated cooling effect due to clouds in the model. The positive BT bias (i.e., excessively large radiance values at the TOA) shown in Figure 2 is consistent with this finding. The spectral region between 1900 and 2100 cm^{-1} is primarily sensitive to air temperature and water vapor in the lower troposphere. Although the

spectral radiance in this interval is extremely low—as it lies in the far tail of the Planck function—small variations in radiance result in large changes in BT. This explains why a positive bias is clearly visible in BT, despite the radiance values being near-zero.

The O_3 absorption band is dominated by a positive bias of about 1.5 K across the tropics and subtropics both in clear and all-sky conditions. However, in the presence of clouds, the positive bias is also present at mid-latitudes. It is important to note that the ozone band is sensitive not only to ozone concentration but also to temperature, both in the stratosphere and in lower troposphere. Thus, it is difficult to fully disentangle the causes of this bias with a simple analysis. A more comprehensive analysis, as presented in Sect. 4, in this case becomes necessary.

In the water vapor band, small differences are observed between clear and cloudy cases: in both cases a positive bias is present between 30°S and 30°N, while at higher latitudes the sign of the bias is reversed. In clear-sky conditions, the positive bias has been related to an underestimation of the water vapor concentration in the EC-Earth3 model (Della Fera et al. 2023). Additional details for the all-sky case will be provided in the analysis of the trends and the subsequent attribution.

2) Assessment of BT trends

Trends are estimated from the monthly average BTs computed over ocean (latitudes from 60°S and 60°N) following the approach presented in Whitburn et al. (2021). We fit the following Fourier series to the monthly averaged brightness temperatures:

$$BT(t, b_0, \mathbf{c}, \mathbf{d}) = a_0 + b_0 t + \sum_{i=1}^{4} \left(c_i \cos(\frac{2\pi t}{T_i}) + d_i \sin(\frac{2\pi t}{T_i}) \right) \tag{7}$$

where a_0 is a constant term, b_0 is the linear trend term and $\mathbf{c}, \mathbf{d}$ are 8 coefficients driving the intensity of the sin and cos terms allowing to represent the atmospheric oscillations with periods T_i: in our case we use annual (12 months), semi-annual (6 months), seasonal (3 months) and also 4 months periodicities. All these terms and coefficients are fitting parameters of our model. We also verified that the linear trend term b_0 obtained using this approach is compatible to that obtained by computing the linear trends to the deseasonalized BT time series. We compute the error associated with the trend b_0 with the bootstrap resampling method presented in Gatz and Smith (1995) and Gardiner et al. (2008).

Once the fitting parameters are determined, the residual deviations—calculated as the difference between the fitted function and the data—are interpreted as the random effects present in the dataset. Thus, the residuals are randomly sampled and added to the initial fit function to generate a new dataset, which is then used to estimate new fitting parameters. The operation is repeated a large number of times in order to have a distribution of the fitting parameters.

The computed errors on the basis of this distribution represent the 95% confidence interval. For each wavenumber, if the trend error bar overlaps the zero value, then the trend is considered not statistically significant.

3) Results

Figure 3 shows the trends calculated with a spectral step of 10 cm^{-1} for EC-Earth3 (red) and IASI (black) brightness temperature (top) and spectral fluxes (bottom) averaged over ocean, between 60°S and 60°N and for all-sky conditions. It is important to note that, to compute the fluxes, here the radiance is assumed to be isotropic, thus, the angular integration is simplified by multiplying the radiance by a factor of π. We acknowledge that this approximation is not entirely accurate, and specific algorithms have been developed to convert spectral radiance into spectral fluxes (Huang et al. 2008; Whitburn et al. 2020). However, as the error introduced by assuming isotropic radiance is systematic, it is unlikely to affect the magnitude of the trends. Providing an accurate estimation of OLR lies beyond the scope of this study; here we limit to solely comparing simulated flux trends with IASI trends across specific spectral bands and with CERES trends over the entire infrared spectrum.

The BT trends (top panel in Figure 3) exhibit positive values across the MIR spectral range starting from 750 cm^{-1}. The peak trend, approximately 0.3 K $decade^{-1}$, is observed in the atmospheric window regions, while in the water vapor band trends are generally around 0.2 K $decade^{-1}$. In contrast, negative trends are observed in the CO_2 band, ranging from 650 to 750 cm^{-1}, with values reaching -0.4 K $decade^{-1}$.

The trends are statistically significant across nearly all wavenumbers, as indicated by the associated error band (shadowed areas in the figure indicate the 95% confidence level). Exceptions are observed in the core of the CO_2 band for IASI and in the CH_4 band for both IASI and EC-Earth3.

Note that the uncertainty of the model trend is generally smaller than that of IASI, as it reflects the error associated with the average of the trends from the three EC-Earth3 simulations.

We have to consider that the trends shown in Figure 3 represent the combined effects of both forcings and feedback mechanisms. Indeed, over the 12-year period from 2008 to 2019, there has been a reduction in the energy emitted at the TOA within the CO_2 absorption band, which is where the most significant radiative forcing occurs. As a consequence, the Earth system has generally increased its longwave radiative emission at TOA, consistent with rising temperatures driven by the Planck feedback.

In general, the climate model successfully reproduces the correct BT and radiance trends. Specifically, in the wing of the CO_2 band and in the atmospheric window (AW1) the trends are well captured by EC-Earth3. The trends are also well represented in the water vapor band and, although here EC-Earth3 slightly overestimates their values, the differences with respect to IASI remain within the error bounds. The most relevant differences in the BT trends of EC-Earth3 and IASI are visible in the core of CO_2 band and in the ozone band where the discrepancies are above 0.2 K decade^{-1}. In both cases the cause of this difference is most likely due to the stratosphere, which is cooling too rapidly in the climate model.

The spectral integration of trends in spectral fluxes (bottom panel of Figure 3) over the whole MIR region [650-2250 cm^{-1}] yields values of 0.46 ± 0.14 W m^{-2} decade^{-1} for EC-Earth3 and 0.40 ± 0.14 W m^{-2} decade^{-1} for IASI. Despite the good agreement of these integrated quantities, significant self-compensating discrepancies exist between model and observations, localized in specific gas absorption bands (see Table 1). Specifically, the EC-Earth3 model overestimates the negative trend in the CO_2 band (-0.098 ± 0.005 vs. -0.086 ± 0.006W m^{-2}decade^{-1}), while underestimating the positive trend in the O_3 band ($+0.078 \pm 0.004$ vs. $+0.096 \pm 0.005$W m^{-2} decade^{-1}). Additionally, the model overestimates the trend in the water vapor band ($+0.107 \pm 0.004$ vs. $+0.062 \pm 0.004$ W m^{-2} decade^{-1}). The model is able to reproduce the trend in OLR within the atmospheric windows, with an integrated value across both regions (AW1+AW2) of 0.323 ± 0.005 W m^{-2} decade^{-1} for EC-Earth3 and 0.294 ± 0.007 W m^{-2} decade^{-1} for IASI, despite the biases observed in the model BT values within these spectral regions.

Since the EC-Earth3 model provides simulated radiances in both the MIR and FIR regions, we can also estimate the trend in OLR over the entire Earth emission spectrum (from 100 to

2600 cm^{-1}) over the ocean, between 60° S and 60° N for the period 2008-2019. The model yields a result of 0.59 ± 0.12 W m^{-2} $decade^{-1}$, closely matching the OLR trend from CERES of 0.56 ± 0.14 W m^{-2} $decade^{-1}$, as derived from the EBAF 4.2 dataset.

To check whether the spectral integration on 10 cm^{-1} intervals adopted in the analysis presented above hides additional information originally present in the IASI high-resolution spectral measurements, we also investigate the trends in the time series of the BT at the 14 high-resolution IASI spectral channels specified in Sect. 2 (see Table 2). Figure 4 summarizes the BT trends (K $decade^{-1}$) in these channels as derived from the EC-Earth3 model and the IASI observations, including their respective 95% confidence intervals. All the trends are statistically significant except for values of IASI at 1326.75 cm^{-1} (CH_4 band) To complete the high-resolution analysis, Figure 5 presents the time series for a subset of four high-resolution IASI channels, while the full set of time series for all 14 channels is shown in Figure 1 of the Supplementary Material. Here, the three red curves represent the BT time series from the EC-Earth3 simulations, each corresponding to a different initial condition (three ensemble members), while the black line represents the BT time series from IASI observations.

Overall, the comparison of the trends in the high-resolution channels confirms the good agreement between model and observations, with the exception of channels that are more sensitive to the stratosphere (667.75 cm^{-1} and 1041 cm^{-1}). The linear BT trend at 667.75 cm^{-1}, shown in Figure 4, and the corresponding time series in Figure 5, highlight the significant challenges the model faces in accurately representing stratospheric temperature and its time evolution. In this channel, the trend derived from the EC-Earth3 simulation is -0.90 K $decade^{-1}$, to be compared to -0.49 K $decade^{-1}$ observed in the IASI data. These values are nearly double as compared to those identified in the low-resolution analysis. This is because the considered channel corresponds to the peak CO_2 absorption. Moving to higher wavenumbers in the wing of the CO_2, the EC-Earth3 performance improves.

As already anticipated, both for the model and IASI at these wavenumbers the BT is decreasing across the analysis period. Of course, this behaviour is not due to a cooling of the troposphere but, as we will better assess in the next section, is actually caused by the combined effect of CO_2 and temperature changes at different altitudes. The channel at 901.50 cm^{-1}, in the atmospheric window, shows a positive trend of 0.31 K $decade^{-1}$. The slight difference with the channel at 871.25 cm^{-1}

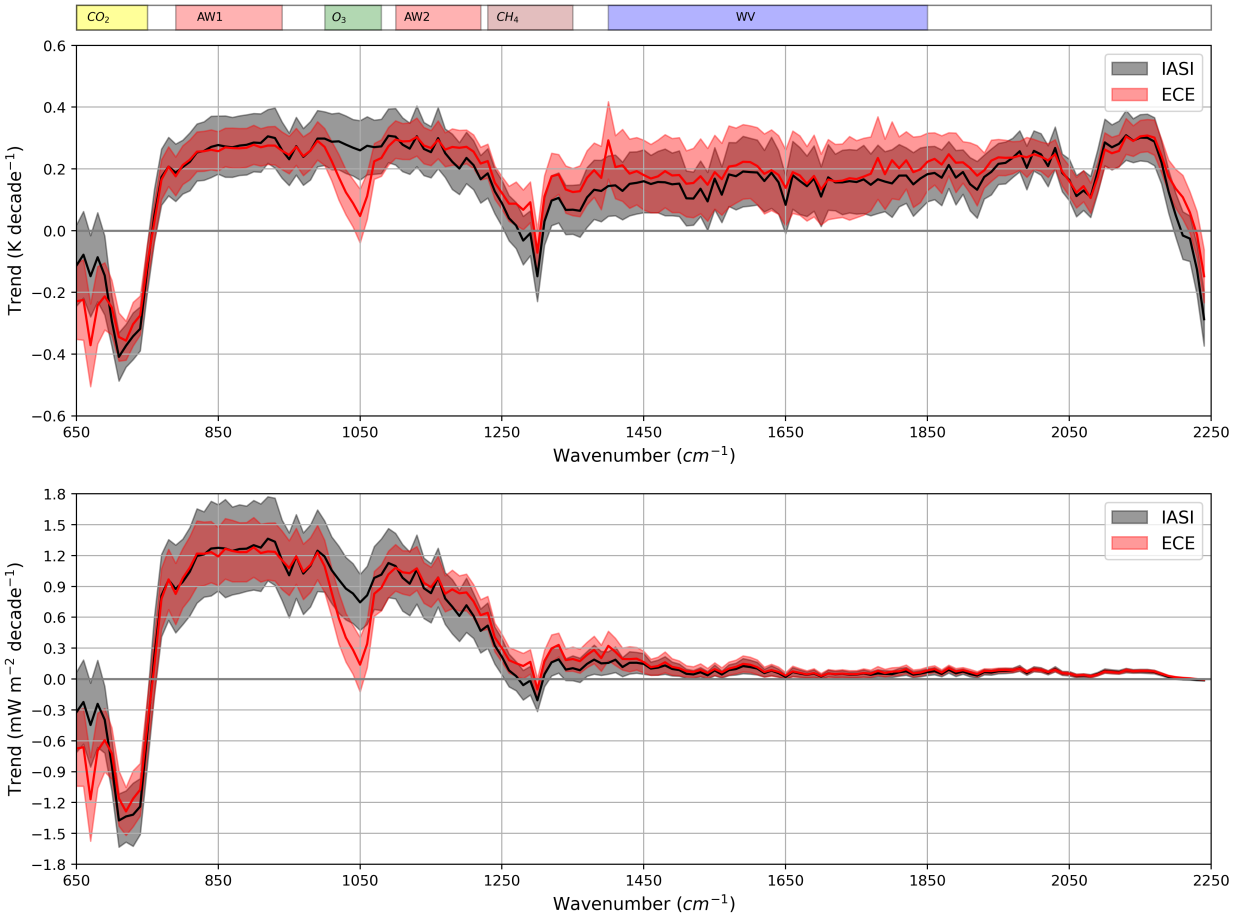

FIG. 3. Comparison of all-sky trends for the EC-Earth3 model (label ECE, red) and IASI (black) in terms of BT (top) and spectral fluxes (bottom) for the period 2008 - 2019. The shaded areas represent the 95% confidence interval associated with the value of the trend.

(see Figure 4), also within the atmospheric window, could be attributed to the different sensitivities of the two channels to water vapor concentration. Indeed, at 901.50 cm^{-1}, the radiance is less affected by water vapor amount and the radiation is emitted by atmospheric layers that are closer to surface. As shown in the time series in Figure 5 panel a) , EC-Earth3 overestimates the BT in this channel by approximately 1 K due to the presence of clouds. Additionally, the amplitude and the periodicity of the EC-Earth3 BT time series differ substantially from those in the observations.

The two selected channels in the ozone band (1014.50 and 1041 cm^{-1}) exhibit contrasting behaviours in the BT trends estimated from the model (Figure 4): the trend in the first channel is positive for both EC-Earth3 and IASI, while in the second channel the EC-Earth3 trend has

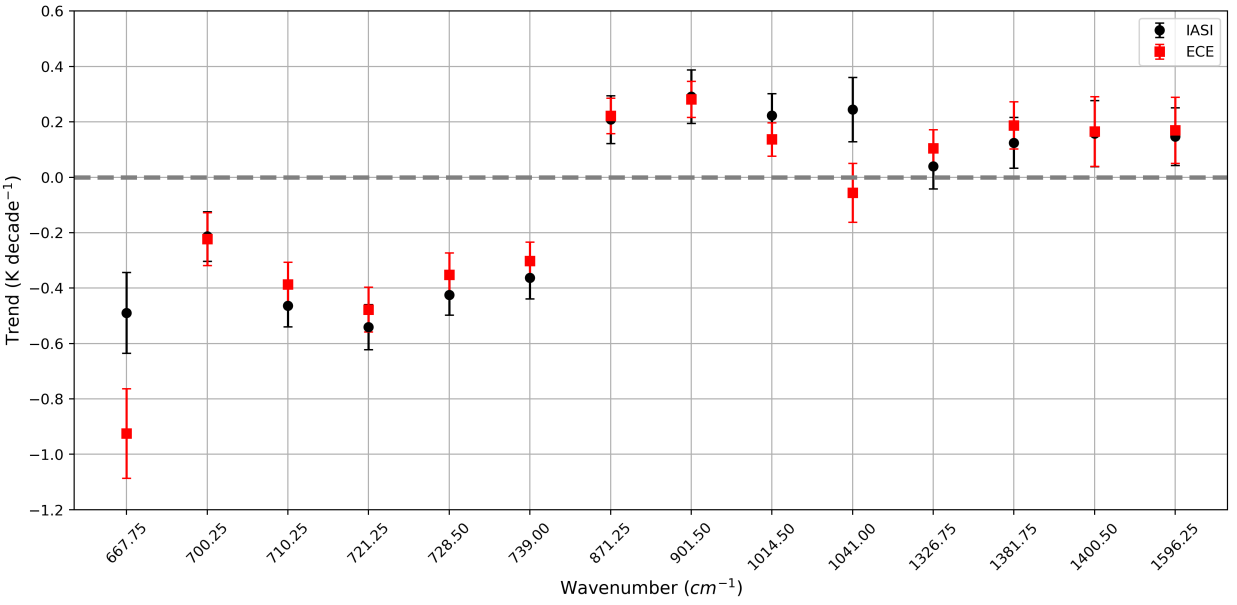

FIG. 4. IASI and EC-Earth3 trends for the high resolution channels selected in Sect. 2. The error bars represent the 95% confidence intervals.

opposite sign as compared to IASI. This is because the radiance emitted at 1041 cm^{-1} primarily originates from the stratosphere, which cools excessively in the climate model, similar to what is observed for the channel at 667.5 cm^{-1} (see also Figure 5 panel a)). In contrast, the radiance at 1014.50 cm^{-1} is more influenced by tropospheric and surface temperatures, leading to a positive trend and better agreement with IASI observations.

The water vapor band is analyzed by selecting four channels (1326.75, 1381.75, 1400.50, and 1596.25 cm^{-1}), with the time series for one of these channels (1400.50 cm^{-1}) presented in Figure 5 panel d).

All the channels, despite their sensitivity to water vapor and temperature at different altitudes (see Table 2), display similar positive trends of approximately 0.2 K decade^{-1}, with the simulated trends closely matching the observed values. Notably, the channel at 1400.50 cm^{-1} is influenced not only by temperature and water vapor in the mid-troposphere but also by methane concentration.

4. Decomposition and attribution of trends

In Section 3, we identified the main spectral biases in the climate model and assessed its ability to replicate the observed trends. Here, we employ a kernel analysis on the simulated spectral

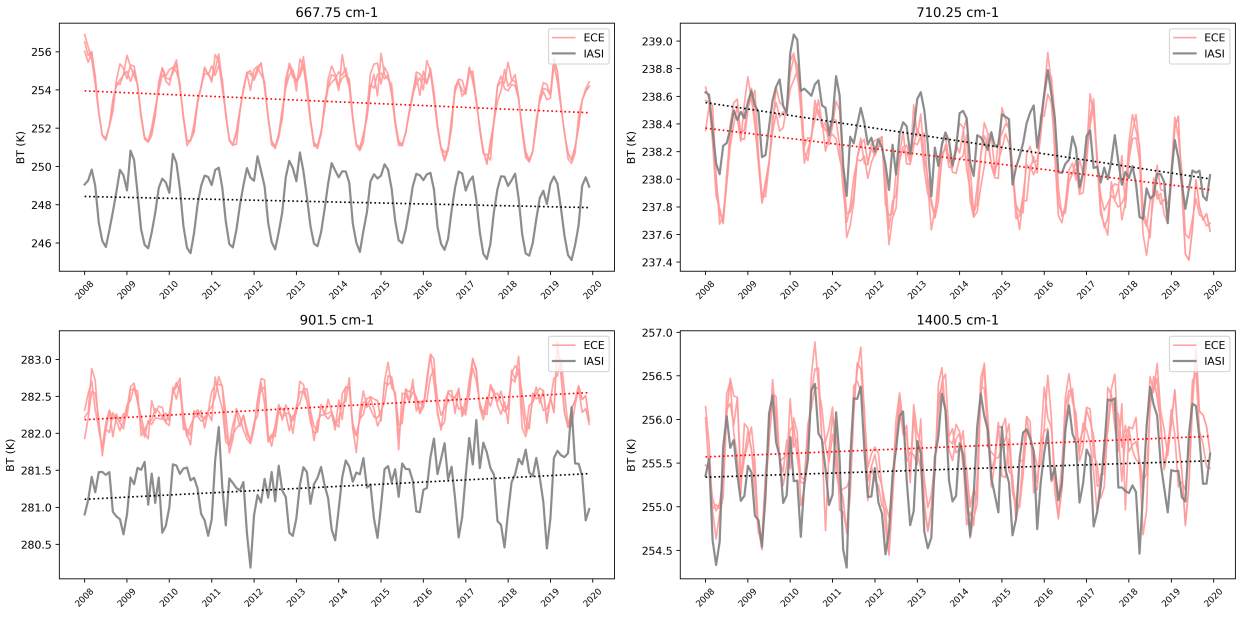

FIG. 5. Time series of Brightness Temperature in four IASI channels (see plot's key). The three red lines represent climate model simulations with different initial conditions, while the dotted lines show the linear component of Equation 7. Note the different vertical scales across the plots

radiances to trace the origins of these trends back to the evolution of key climate variables. The application of spectral kernels enables the separation of forcings and feedbacks. Moreover, given the good agreement between the model and the observations, lessons learnt from the synthetic radiances can facilitate the attribution of the radiance trends observed by IASI.

In Subsection 1, we describe the kernel technique. Subsection 2 presents the results.

1) COMPUTATION OF SPECTRAL KERNELS

To decompose the trends of spectrally resolved radiances, we use the following linear approximation:

$$\Delta \mathbf{L}_\nu(t_i) = \mathbf{K}_\nu(t_i)\Delta \mathbf{x}(t_i) + \epsilon_\nu(t_i). \tag{8}$$

In this expression, $\Delta \mathbf{L}_\nu(t_i)$ is a vector whose elements represent the spectral (ν) anomalies of the radiances of the month t_i with respect to the monthly climatology computed over the period 2008-2019. $\mathbf{K}_\nu(t_i)$ is the spectral kernels matrix. Each column of this matrix contains the derivative of

the spectral radiance with respect to a relevant climate variable (element of vector $\mathbf{x}$) to which the radiance is sensitive. Radiance derivatives are evaluated at the monthly mean atmospheric state for each month t_i during the 2008–2010 period, and subsequently averaged to obtain representative monthly mean kernels. $\mathbf{\Delta x}(t_i)$ is a vector containing the anomalies of the mean climate variables at month t_i, with respect to monthly climatology of the whole period 2008-2019. Finally, $\epsilon_\nu(t_i)$ is a residual contribution term.

We compute the spectral kernels with the radiative transfer model RTTOV (Radiative Transfer for Tiros-N Operational Vertical Sounder (TOVS) (Matricardi 2009; Hocking et al. 2021) both in clear- ($\mathbf{K}_{\nu,\mathrm{clear}}$) and all-sky ($\mathbf{K}_{\nu,\mathrm{cloudy}}$) conditions (Soden et al. 2008; Huang et al. 2014). Initially developed to simulate the Tiros-N Operational Vertical Sounder (TOVS) observations, RTTOV is now able to perform simulations of a large variety of sensors working in different spectral ranges, from visible to microwaves. RTTOV is based on a set of pre-computed transmittances already convolved with the instrumental response functions. This aspect makes RTTOV extremely fast and particularly suitable for simulations based on large set of atmospheric profiles. We use a specific RTTOV routine, called RTTOV-K, to compute the derivatives of the IASI radiances with respect to the following climate variables:

$$\mathbf{x} = \begin{pmatrix} \mathbf{T}(p) \\ T_s \\ \mathbf{x}_{\mathrm{H_2O}}(p) \\ \mathbf{x}_{\mathrm{CO_2}}(p) \\ \mathbf{x}_{\mathrm{O_3}}(p) \\ \mathbf{x}_{\mathrm{CH_4}}(p) \\ \mathbf{x}_{\mathrm{N_2O}}(p) \end{pmatrix} \tag{9}$$

This symbology indicates that our state vector $\mathbf{x}$ contains the temperature profile ($\mathbf{T}(p)$), the surface temperature T_s, and the vertical concentration profiles of the following gases: water vapor (H_2O), ozone (O_3), carbon dioxide (CO_2), methane (CH_4) and nitrous oxide (N_2O).

The anomalies $\mathbf{\Delta x}(t_i)$ are computed from the EC-Earth3 atmospheric profiles. Regarding the derivatives in $\mathbf{K}_\nu(t_i)$, for each month of the year, for this analysis they are computed with RTTOV at the average atmosphere of the actual month in the first three years (2008, 2009, 2010) of the

considered period, from the ERA-5 reanalysis, preliminarily interpolated to an horizontal grid of 2.5°x2.5° and 17 vertical pressure levels from 1000 hPa to 10 hPa.

The effect of clouds on radiances is computed as shown in Huang et al. (2024). First, the unexplained part of the radiance in clear-sky conditions is computed:

$$\epsilon_{\nu,\text{clear}}(t_i) = \mathbf{\Delta L}_{\nu,\text{clear}}(t_i) - \mathbf{K}_{\nu,\text{clear}}(t_i)\mathbf{\Delta x}(t_i) \tag{10}$$

Then, for each month t_i, the radiance anomalies due to clouds ($\delta\mathbf{c}_\nu(t_i)$) are obtained as a corrected residual term, adjusted by removing from the all-sky radiances the residual term obtained in clear-sky conditions. Formally:

$$\delta\mathbf{c}_\nu(t_i) = \mathbf{\Delta L}_{\nu,\text{cloudy}}(t_i) - \mathbf{K}_{\nu,\text{cloudy}}(t_i)\mathbf{\Delta x}(t_i) - \epsilon_{\nu,\text{clear}}(t_i) \tag{11}$$

2) Results

The top panel of Figure 6 illustrates the trend of the radiance anomaly for the spectral interval from 650 to 2250 cm^{-1}, integrated over the global ocean between 60° S and 60°N. It presents the mean of the trends obtained from the set of the EC-Earth3 model simulations (red), the trend derived from the observed IASI radiances (black), and the reconstruction obtained from the kernel analysis (green). This reconstruction is achieved by summing the radiative contributions from the different variables shown in the bottom panel of Figure 6, which are calculated as the product of the spectral kernels $\mathbf{K}_{\nu,\text{cloudy}}$ and the trends of the corresponding variable anomalies $\mathbf{\Delta x}$. The influence of clouds on radiance anomalies is taken into account as described in Equation 11.

The trend reconstructed using the kernel analysis closely matches the radiance trend simulated by EC-Earth3, including under clear-sky conditions (see Figure 2 in the Supplementary Material). Since the climate model profiles are used to reconstruct the trend with the kernels, this confirms that the linear approximation of Equation 8 can reproduce the original trends, even if it does not accurately reproduce the individual monthly radiance anomalies. In particular, there is an excellent match of EC-Earth3 and kernel-derived trends in the wing of the CO_2 band and in the O_3 band, as well as in the atmospheric window regions. The largest discrepancies are observed in the core of the CO_2 band, in the water vapor band and in the methane absorption band, where the trends estimated by the kernel analysis are lower than that resulting from EC-Earth3 simulations. Across

the entire water vapor band, the contributions of temperature and water vapor to the trend nearly offset each other, resulting in an almost zero net trend. This behaviour can be explained on the basis of the "Simpson's Law", which states that, within the water vapor band, the OLR remains largely unaffected by variations in surface temperature under the assumption of fixed relative humidity (RH) (Jeevanjee et al. 2021). Since RH is not expected to vary significantly under climate change (Ingram 2010), and given that Simpson's Law is a first-order approximation, the anti-correlation between temperature and water vapor may be more pronounced in the kernel analysis, which is also based on a linear approximation. Note that, within our 'Simpsonian' framework, we also expect a near-perfect cancellation between temperature and water vapor contributions in the FIR, which is dominated by the rotational water vapor absorption band and is excluded from our analysis. However, recent studies have shown that surface warming leads to increased emission even within water vapor absorption bands, resulting in a critical stabilizing effect on the climate, an effect not captured by traditional 'Simpsonian' models (Raghuraman et al. 2023; Feng et al. 2023). Moreover, the clear-sky longwave feedback is primarily governed by the surface response when the near-surface air temperature is low ($T < 270K$), whereas atmospheric processes become increasingly important at higher temperatures (Roemer and Buehler 2025). Non-linear effects could also explain the mismatch between the EC-Earth3 trends and the kernel-derived trends in the core of the CO_2 band.

The good agreement between EC-Earth3 and IASI trends, as also highlighted in the previous Section, and the accurate reconstruction of the EC-Earth3 trends achieved through kernel analysis, enable a reliable attribution of the underlying causes of these trends. For the sake of clarity, in the bottom panel of Figure 6, a negative trend in spectral radiances signifies a reduction in the emitted OLR at the TOA, indicating a positive forcing or a positive (de-stabilizing) climate feedback. Conversely, a positive trend in spectral radiances represents an increase in emitted energy toward the TOA, signifying a negative forcing or a negative (stabilizing) climate feedback.

To give a synthetic picture of the individual contributions to the trend, the spectral forcings and feedbacks of Figure 6 have been integrated across the analyzed spectral range ([650-2250 cm^{-1}]) and converted to fluxes under the approximation of isotropic radiance, and summarized in Table 3. The CO_2 forcing (dark red line in Figure 6) represents the most significant forcing impacting the climate system (see left panel in Table 3). This positive forcing is partially offset by a negative

component within the core of the CO_2 band. As already discussed, radiance at these frequencies primarily originates from the stratosphere. The increase in CO_2 concentration raises the emission level to higher altitudes, enhancing energy emission toward the TOA due to the temperature rise with altitude in the stratosphere. In the troposphere, the same process - the increase of the emission level altitude - produces the opposite effect, as temperature decreases with altitude. The estimation of CO_2 forcing in Table 3 does not account for its total effect, as the FIR spectral range is not considered. CH_4 (violet line) is the second strongest positive forcing, while the N_2O forcing (dashed olive line) is approximately half the magnitude of the CH_4 forcing. Unlike the other gases, the net effect of ozone (green line) on the OLR trend, although minimal, is positive (negative forcing). This positive trend arises from the influence of ozone concentration changes in the upper troposphere and stratosphere on radiation (see Figure 3 of the Supplementary Material).

As represented in Figure 6 and summarized in Table 3, the planetary feedback is dominated by the negative Planck feedback, driven by increases in air temperature (blue line) and surface temperature (orange line). Note that in this analysis, we do not distinguish the lapse rate contribution within the Planck feedback.

The positive water vapor feedback hinders Earth's cooling, as the increased atmospheric water vapor traps more energy within the system (light blue line). The cloud feedback is also positive, resulting in a negative influence on the trend (grey line). Although this feedback is primarily confined to the atmospheric window regions, its magnitude is significant.

Forcing Trend	($mW \cdot m^{-2} decade^{-1}$)
CO_2	+129.8
CH_4	+37.7
O_3	-6.1
N_2O	+19.7

Feedback Trend	($mW \cdot m^{-2} decade^{-1}$)
T	-946.4
T_s	-349.9
H_2O	+537.2
Clouds	+212.6

TABLE 3. Trends of integrated spectral forcings (left) and feedbacks (right) across the mid-infrared spectral range [650-2250 cm^{-1}]. Positive values represent a trend of energy gain for the Earth's system, while negative values indicate a trend of energy loss.

To further explore the role of climate variables in the radiation trends, Figure 7 presents the time series of observed (dashed black lines), simulated (red lines) and kernel-reconstructed (green lines) radiance anomalies in four of the selected high-resolution IASI channels (see Fig. 7 panels a), b),

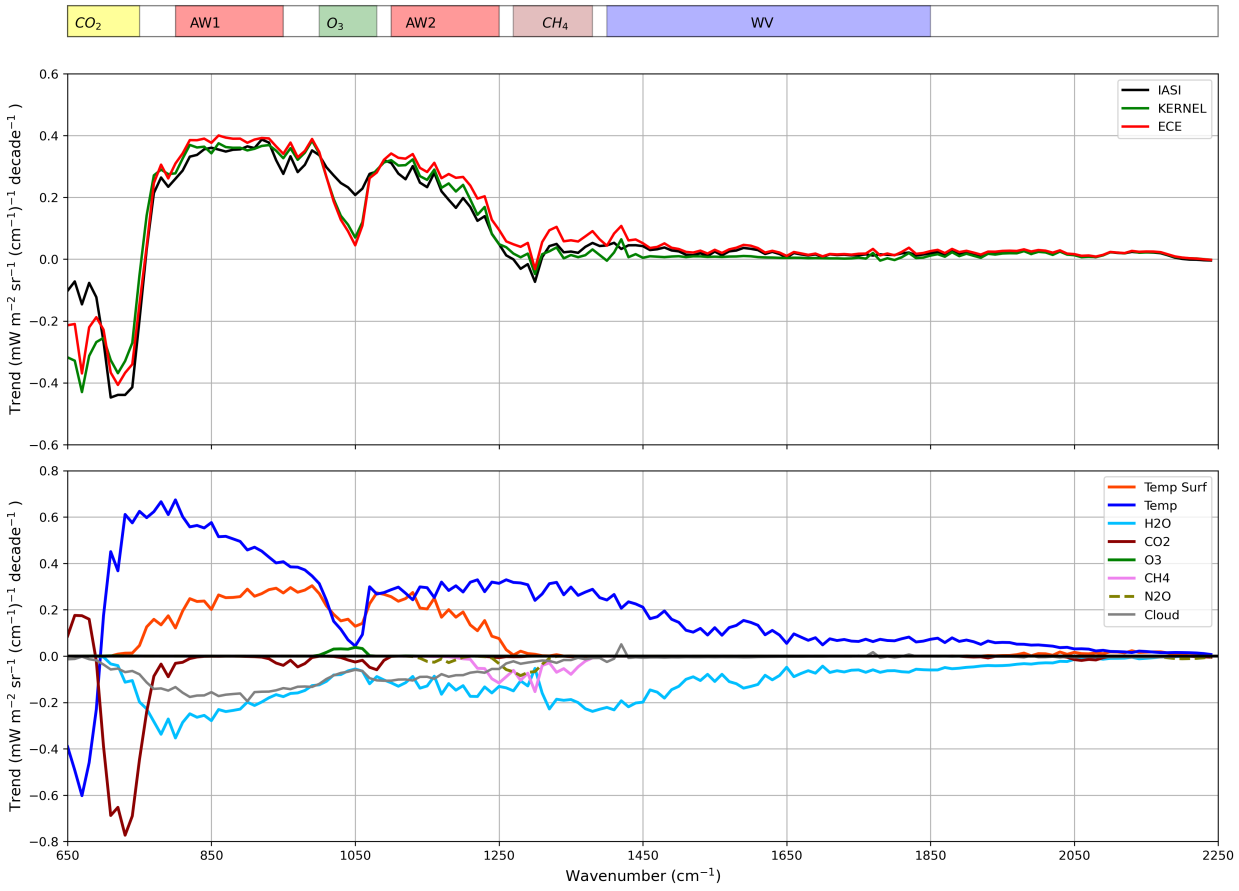

590 FIG. 6. Spectral radiance trend computed from model simulations, its reconstruction using spectral kernels
591 and the observed radiance trend from IASI (top). The various radiative contributions from different variables
592 are shown (bottom).

604 e) and f)). Additionally, panels c), d), g) and h) of Fig. 7 show the relevant terms contributing to
605 the kernel analysis reconstruction. The various terms are identified by the key at the bottom of the
606 figure. The vertical profiles of temperature and of water vapor give an important contribution to
607 the radiance anomalies thus, in Figures 8 and 9, we show the breakdown of these contributions by
608 pressure level (colour code). Figures 8 and 9 refer to temperature and water vapor contributions,
609 respectively. Each figure panel refers to a specific frequency channel, as indicated in the panel's
610 key.

614 The linear approximation used in the kernel analysis generally reproduces quite accurately also
615 the radiance anomalies of the high-resolution channels. The most significant discrepancies between
616 the climate model simulations and the kernel-reconstructed radiance anomalies are found at 667.75

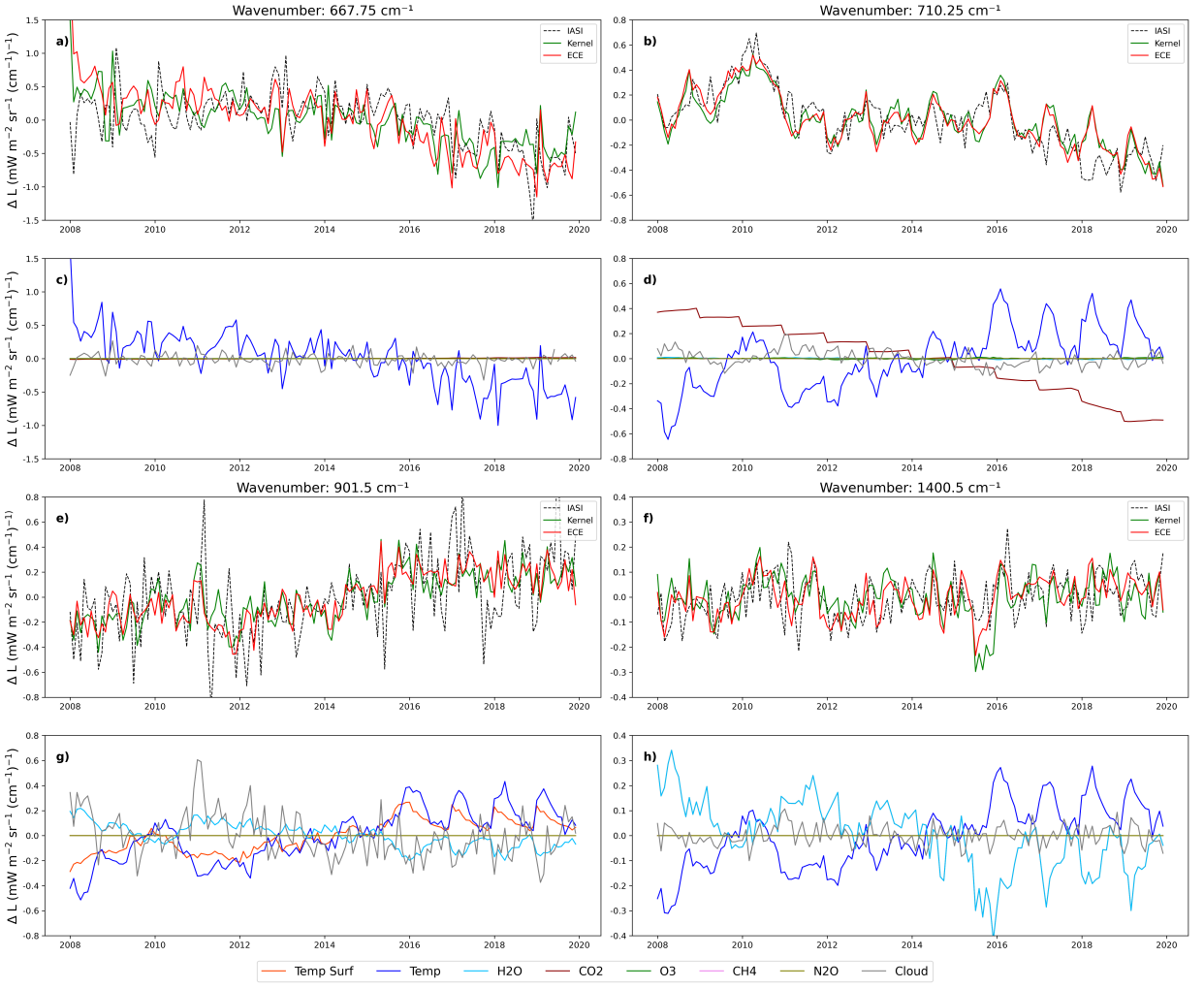

593 FIG. 7. For each of the 4 considered IASI channels (667.75, 710.25, 901.5 and 1400.5 cm^{-1}) panels a),
594 b), e) and f) show the radiance anomalies time series from IASI (black), from model simulations (red) and
595 their reconstruction using spectral kernels (green). For each of the channels, panels c), d), g) and h) show the
596 contributions to the kernel-reconstructed radiance anomalies from the different variables indicated in the color
597 code key at the bottom of the figure.

617 and 1400.5 cm^{-1} (see panels a) and f) of Fig. 7). At 667.75 cm^{-1}, the kernel analysis indicates
618 that the dominant factor driving the negative trend in spectral radiances anomalies is the air
619 temperature (blue line) (Figure 7). More in detail, Figure 8 (panel a)) confirms that in this channel
620 the radiance at TOA is influenced solely by the negative trend in stratospheric temperature. The
621 cooling of the stratosphere is a well-documented phenomenon in the literature. Over the past
622 three decades, a continuous decrease in stratospheric temperatures has been observed, primarily

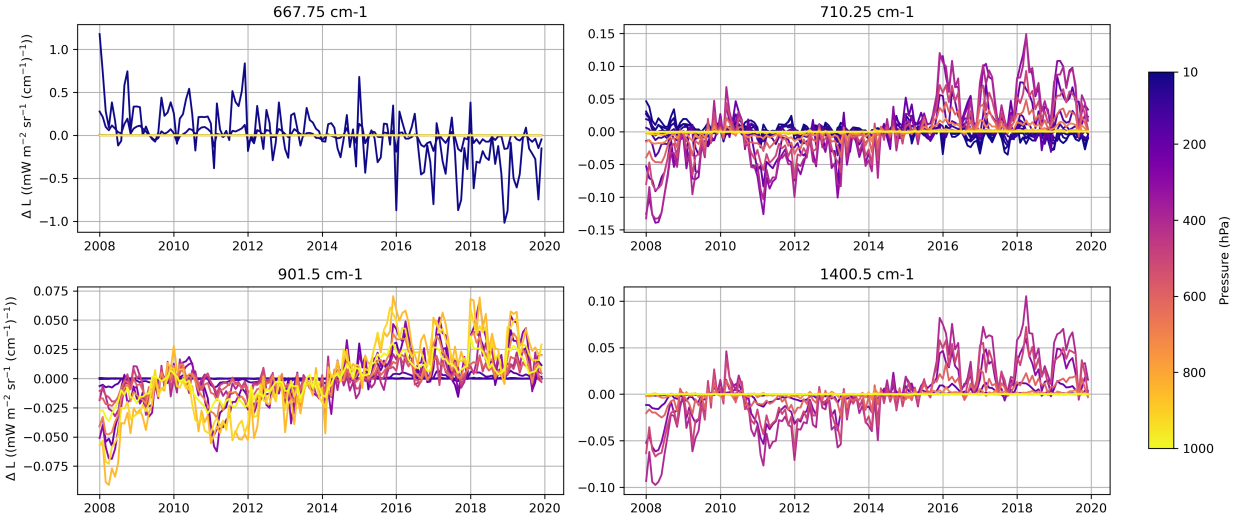

611 FIG. 8. Contributions of temperature at different atmospheric layers (see color code of lines) to radiance
612 anomalies. The four panels refer to specific channels, as indicated in the panels title. Note the different vertical
613 scales across the plots.

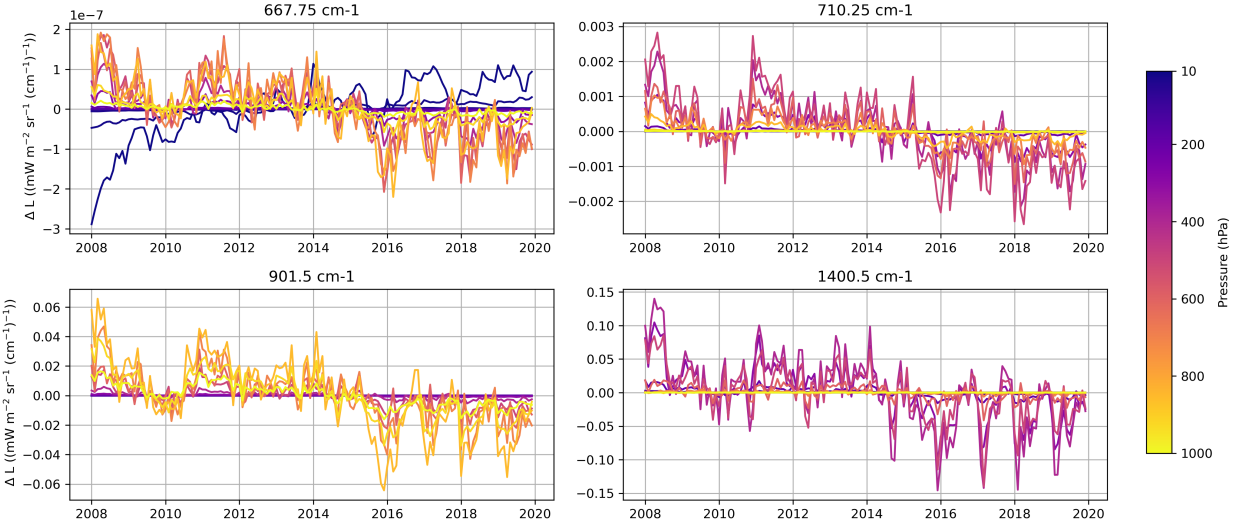

FIG. 9. Same as Fig. 8 but for water vapor. Note the different vertical scales across the plots.

623 attributed to anthropogenic factors, namely ozone loss and increase of other greenhouse gases in
624 the stratosphere (Ramaswamy et al. 2001, 2006; Pan et al. 2017). As noted in the previous section,
625 the EC-Earth3 model significantly overestimates the stratospheric cooling, exhibiting a decrease
626 in BTs nearly twice as steep as the observed values. Additionally, this channel exhibits minimal
627 sensitivity to water vapor concentration (see Figure 9 panel a)). Although the effect of stratospheric

water vapor on radiance is about seven orders of magnitude smaller than that of temperature, we see that it is positive, compatible with an increase in water vapor at higher altitudes in the stratosphere.

The channel at 710.25 cm^{-1} shows a less pronounced negative trend in spectral radiance as compared to the channel at 667.75 cm^{-1}. Indeed, Figures 7 (panels b) and d)) and 8 (panel b)) reveal that in this case the negative radiance trend arises mainly from the positive trend of CO_2 concentration. Note that the step-like behaviour of the radiative anomaly due to CO_2 is the result of calculating monthly anomalies of CO_2 concentration that increases almost linearly over the analyzed period. For this channel, the air temperature contribution to the radiance anomaly trend derives both from the negative trend of the stratospheric temperature and from the positive trend of tropospheric temperature (see panel b) of Figure 8). The negative radiance trend driven by CO_2 is consistent with the rising concentration of this gas in the troposphere. Indeed, the increase in CO_2 concentration implies more energy trapped in the system, leading to a shift to colder, higher altitudes of the emission level for this channel, causing a decrease in the radiance at TOA. The same effect is determined by the increase of water vapor in the upper troposphere (see panel b) of Figure 9). Finally, the channel at 710.25 cm^{-1}, like the channel at 667.75 cm^{-1}, is minimally affected by clouds.

The channel at 901.5 cm^{-1} is within the atmospheric window, where the radiance is very sensitive to both surface temperature and air temperature in the lowest atmospheric layers. The effects of the temperature and water vapor trends on the trend of radiance are opposite in sign. In the atmospheric window, the role of clouds becomes crucial, and for the 901.5 cm^{-1} channel, their effect is comparable to that of all other variables (panels e) and g) of Figure 7). Note that, while in the presence of clouds we see discrepancies both in the amplitude and in the periodicity of the EC-Earth simulated and IASI-measured radiance anomalies, this discrepancy does not show up in the trends comparison.

The inverse effect of temperature and water vapor found in the 901.5 cm^{-1} and 710.25 cm^{-1} channels is even more evident in the water vapor band, at 1400 cm^{-1}. Here water vapor and temperature supply contributions to the trend in radiances that are opposite-in-sign and of similar amplitude (see panels f) and h) of Figure 7). The kernel analysis is also applied to the other IASI channels of Table 2. The results of the spectral decomposition are plotted in Figures 4,5 and 6 of the Supplementary Material.

5. Discussion and Conclusions

In this study, trends in spectrally resolved radiances from the IASI instrument for the period 2008–2019 are compared with trends in synthetic outgoing longwave radiances generated by the EC-Earth3 climate model. The synthetic radiances are simulated in runtime using a IASI simulator integrated into the EC-Earth3 climate model (Della Fera et al. 2023), which has been updated and optimized in this work to operate under all-sky conditions.

The trend comparison is performed after assessing the main spectral biases in the model-simulated spectra, averaged in 10 cm^{-1} intervals (Figure 3). Additionally, high-resolution synthetic radiances are analyzed at a set of IASI channels selected for being the most sensitive to key climate variables at different altitudes. The EC-Earth3 climate model reproduces quite accurately the observed trends in spectrally resolved radiances measured by IASI across most of the mid-infrared spectral range. Significant discrepancies are observed in the core of the CO_2 band and in the O_3 band, which are attributed to an overestimation of stratospheric cooling in the model. While the BT trend of EC-Earth at 667.75 cm^{-1} is about -0.9 K $decade^{-1}$, IASI shows a BT trend of approximately -0.5 K $decade^{-1}$. In this channel, IASI BT trend is close to the value found in Pan et al. (2017) from AIRS data (-0.58 K $decade^{-1}$) analyzed across the years 2002-2013.

Smaller differences between observed and simulated radiance trends are found in the wing of the CO_2 band, in the water vapor band, and in the atmospheric windows. The sign of the bias changes across the OLR spectral range, thus largely self-compensating and giving wavenumber-integrated trends that match well with those obtained from CERES measurements over the same period.

We then employ a spectral kernel analysis to quantify the impact of the individual geophysical variables on the radiance trends. The kernel analysis is a linear approximation in which the radiance anomalies are obtained as the product of the spectral kernel—the derivative of the radiances with respect to the climate variables of interest— by the anomalies of the same variables. The good representation of IASI radiance trends by the climate model, along with an understanding of the model's biases, allows us to decompose and attribute the observed radiance trends to specific variables and quantify the spectral forcing trends and feedbacks over the period considered (2008-2019) (Figure 6). It is important to note that, while the kernel decomposition effectively captures the overall trend, the linear approximation does not accurately reproduce the individual monthly

radiance anomalies, meaning that some finer details may not be fully captured by this linear approach.

As expected, the main forcing to the system is located within the CO_2 absorption band (650–750 cm^{-1}). In the wing of this band (690–750 cm^{-1}), we observe a strong negative BT trend of about -0.4 K $decade^{-1}$. In agreement with the findings of Raghuraman et al. (2023), this trend arises from the combined effects of reduced radiation escaping to the TOA (an energy gain for the system) caused by the increase in CO_2 concentration, and a compensating positive temperature response, which enhances emission toward the TOA (negative Plank feedback). Conversely, in the core of the CO_2 band (650–690 cm^{-1}), the negative trend is due to the combined effects of stratospheric cooling, which reduces the energy emitted to space, and the increased CO_2 concentration, which enhances the emission in the stratosphere.

The Planck feedback, given by the rise in air and surface temperatures, is the strongest stabilizing mechanism for the planet's energy budget. Except for the core of the CO_2 band, this feedback affects the whole mid-infrared wavenumbers determining a positive trend in spectral radiances. This trend reaches its maximum value of approximately +0.3 K $decade^{-1}$ in the atmospheric windows (800-950 cm^{-1} and 1100-1250 cm^{-1}). The water vapor feedback, driven by the increased water vapor concentration in the atmosphere and responsible for a negative contribution to the radiance trend, is strongly anti-correlated with the Planck feedback. This is particularly evident in the water vapor absorption band, where the two feedbacks nearly compensate each other. The global ocean comparison conducted in this study likely masks the pronounced latitudinal variations in OLR trends present within the water vapor band, as highlighted in IASI spectral OLR trends presented in Whitburn et al. (2021). Clouds, whose effect is computed here as a residual with respect to the clear-sky radiation, act as a positive feedback in the longwave spectrum by trapping more energy in the system, and their effect on radiation is primarily observed in the atmospheric windows.

Other GHGs, such as CH_4 and N_2O, tend to reduce the OLR at TOA in the range 1200-1400 cm^{-1}. However, at these frequencies, the radiation trend remains positive due to the dominant effect of the Planck feedback. Finally, although the EC-Earth3 and IASI OLR trends differ significantly within the ozone band ($\approx 1030\,cm^{-1}$) due to the excessive stratospheric cooling of the model, in

both cases the trend is slightly positive. Thus, unlike other gases, variation of ozone concentration exerts a net positive effect on radiation trend.

This comparison highlights the fundamental role of spectral OLR measurements (Level 1 data) in climate studies. Indeed, spectral radiance contains plenty of information about atmospheric and surface properties, providing a new perspective on the study of forcings and feedbacks within the climate system. The main challenge lies in isolating and identifying the individual contributions from various climatic components that are integrated within the spectral signal. While using only Level 2 products (such as temperature, water vapor profiles, etc.) obtained from retrieval procedures might seem like a more efficient approach, these products are always derived with an a priori profile, which can introduce biases into the analysis. In contrast, the combined use of Level 1 and Level 2 data allows for a comprehensive study of the evolution of key climate variables.

In this context, the study shows how the combined use of radiance trends and their decomposition through spectral kernel analysis provides a complete framework to monitor the evolution of the climate system and to verify the accuracy of climate model projections. While the current study focuses on radiance trends over the global ocean, more detailed analyses could be performed at regional scales to explore specific climate phenomena, which we plan to address in future studies.

Acknowledgments. The authors acknowledge CINECA and ECMWF for proving computational resources, and EUMETSAT for making available the huge amount of L1c IASI data through the European Weather Cloud service (EWC). The $\sigma - IASI$ was made available by its authors (see data availability statement). Finally, this work has been carried out in the framework of the EMM - Earth-Moon-Mars project (PNRR, Mission 4, Component 2, Investment 3.1, Project IR000038, CUPC53C22000870006) and of the MC-FORUM project (Meteo and Climate exploitation of FORUM), funded by the Italian Space Agency from January 2024. The authors thank the three anonymous referees for their contributions to improving the clarity and content of the paper.

Data availability statement. Permission to access the EC-Earth3 source code can be requested from the EC-Earth3 community via the EC-Earth3 website (`http://www.EC-Earth3.org/`, EC-Earth3 consortium, 2019a) and may be granted if a corresponding software license agreement is signed with ECMWF.

The $\sigma - IASI$ code is available on Zenodo (`https://doi.org/10.5281/zenodo.7019991`)

The RTTOV code can be obtained from EUMETSAT NWP-SAF facility (`https://nwp-saf.eumetsat.int/site/software/rttov/download/`).

IASI data can be downloaded from EUMETSAT Data Store (`https://data.eumetsat.int/`).

The spectral kernels used in this study are publicly available on Zenodo. (`https://doi.org/10.5281/zenodo.15487604`)

The tools used to compute the radiance anomalies from the kernels are available in the following GitHub repository : `https://github.com/fedef17/SpectFbCalc`

References

Amato, U., G. Masiello, C. Serio, and M. Viggiano, 2002: The σ-iasi code for the calculation of infrared atmospheric radiance and its derivatives. *Environmental Modelling & Software*, **17 (7)**, 651–667.

Anderson, G. P., S. A. Clough, F. Kneizys, J. H. Chetwynd, and E. P. Shettle, 1986: Afgl atmospheric constituent profiles (0.120 km). Tech. rep., Air Force Geophysics Lab Hanscom AFB MA.

Aumann, H. H., and C. R. Miller, 1995: Atmospheric infrared sounder (airs) on the earth observing system. *Advanced and Next-Generation Satellites*, SPIE, Vol. 2583, 332–343.

Barkstrom, B. R., 1984: The earth radiation budget experiment (erbe). *Bulletin of the american meteorological society*, **65 (11)**, 1170–1185.

Bloom, H. J., 2001: The cross-track infrared sounder (cris): a sensor for operational meteorological remote sensing. *IGARSS 2001. Scanning the Present and Resolving the Future. Proceedings. IEEE 2001 International Geoscience and Remote Sensing Symposium (Cat. No. 01CH37217)*, IEEE, Vol. 3, 1341–1343.

Bodas-Salcedo, A., and Coauthors, 2011: Cosp: Satellite simulation software for model assessment. *Bulletin of the American Meteorological Society*, **92 (8)**, 1023–1043.

Chou, M.-D., K.-T. Lee, S.-C. Tsay, and Q. Fu, 1999: Parameterization for cloud longwave scattering for use in atmospheric models. *Journal of climate*, **12 (1)**, 159–169.

Crevoisier, C., and Coauthors, 2014: Towards iasi-new generation (iasi-ng): Impact of improved spectral resolution and radiometric noise on the retrieval of thermodynamic, chemistry and climate variables. *Atmospheric Measurement Techniques*, **7 (12)**, 4367–4385.

Della Fera, S., F. Fabiano, P. Raspollini, M. Ridolfi, U. Cortesi, F. Barbara, and J. von Hardenberg, 2023: On the use of infrared atmospheric sounding interferometer (iasi) spectrally resolved radiances to test the ec-earth climate model (v3. 3.3) in clear-sky conditions. *Geoscientific Model Development*, **16 (4)**, 1379–1394.

Döscher, R., and Coauthors, 2021: The ec-earth3 earth system model for the climate model intercomparison project 6. *Geoscientific Model Development Discussions*, **2021**, 1–90.

Edwards, P., and D. Pawlak, 2000: Metop: The space segment for eumetsat's polar system. *ESA bulletin*, 7–18.

EUMETSAT, 2018: IASI Level 1C Climate Data Record Release 1 - Metop-A. European Organisation for the Exploitation of Meteorological Satellites, URL https://doi.org/10.15770/EUM_SEC_CLM_0014, https://doi.org/10.15770/EUM_SEC_CLM_0014.

Eyring, V., S. Bony, G. A. Meehl, C. A. Senior, B. Stevens, R. J. Stouffer, and K. E. Taylor, 2016: Overview of the coupled model intercomparison project phase 6 (cmip6) experimental design and organization. *Geoscientific Model Development*, **9 (5)**, 1937–1958.

Feng, J., D. Paynter, and R. Menzel, 2023: How a stable greenhouse effect on earth is maintained under global warming. *Journal of Geophysical Research: Atmospheres*, **128 (9)**, e2022JD038 124.

Gardiner, T., and Coauthors, 2008: Trend analysis of greenhouse gases over europe measured by a network of ground-based remote ftir instruments. *Atmospheric Chemistry and Physics*, **8 (22)**, 6719–6727.

Gatz, D. F., and L. Smith, 1995: The standard error of a weighted mean concentration—i. bootstrapping vs other methods. *Atmospheric Environment*, **29 (11)**, 1185–1193.

Gregory, J. M., and Coauthors, 2004: A new method for diagnosing radiative forcing and climate sensitivity. *Geophysical research letters*, **31 (3)**.

Haarsma, R., and Coauthors, 2020: Highresmip versions of ec-earth: Ec-earth3p and ec-earth3p-hr. description, model performance, data handling and validation. *Geoscientific Model Development Discussions*, **2020**, 1–37.

Harries, J., and Coauthors, 2008: The far-infrared earth. *Reviews of Geophysics*, **46 (4)**.

Hilton, F., and Coauthors, 2012: Hyperspectral earth observation from iasi: Five years of accomplishments. *bulletin of the american meteorological Society*, **93 (3)**, 347–370.

Hocking, J., J. Vidot, P. Brunel, P. Roquet, B. Silveira, E. Turner, and C. Lupu, 2021: A new gas absorption optical depth parameterisation for rttov version 13. *Geoscientific Model Development*, **14 (5)**, 2899–2915.

Hogan, R. J., and A. J. Illingworth, 2000: Deriving cloud overlap statistics from radar. *Quarterly Journal of the Royal Meteorological Society*, **126 (569)**, 2903–2909.

Hogan, R. J., and Coauthors, 2017: *Radiation in numerical weather prediction*. European Centre for Medium-Range Weather Forecasts.

Hourdin, F., and Coauthors, 2017: The art and science of climate model tuning. *Bulletin of the American Meteorological Society*, **98 (3)**, 589–602.

Huang, H., Y. Huang, Q. Wei, and Y. Hu, 2024: Band-by-band spectral radiative kernels based on the era5 reanalysis. *Scientific Data*, **11 (1)**, 237.

Huang, X., X. Chen, B. J. Soden, and X. Liu, 2014: The spectral dimension of longwave feedback in the cmip3 and cmip5 experiments. *Geophysical Research Letters*, **41 (22)**, 7830–7837.

Huang, X., V. Ramaswamy, and M. D. Schwarzkopf, 2006: Quantification of the source of errors in am2 simulated tropical clear-sky outgoing longwave radiation. *Journal of Geophysical Research: Atmospheres*, **111 (D14)**.

Huang, X., W. Yang, N. G. Loeb, and V. Ramaswamy, 2008: Spectrally resolved fluxes derived from collocated airs and ceres measurements and their application in model evaluation: Clear sky over the tropical oceans. *Journal of Geophysical Research: Atmospheres*, **113 (D9)**.

Huang, X., and Coauthors, 2022: A synopsis of airs global-mean clear-sky radiance trends from 2003 to 2020. *Journal of Geophysical Research: Atmospheres*, **127 (24)**, e2022JD037 598.

Huang, Y., V. Ramaswamy, X. Huang, Q. Fu, and C. Bardeen, 2007: A strict test in climate modeling with spectrally resolved radiances: Gcm simulation versus airs observations. *Geophysical Research Letters*, **34 (24)**.

Ingram, W., 2010: A very simple model for the water vapour feedback on climate change. *Quarterly Journal of the Royal Meteorological Society: A journal of the atmospheric sciences, applied meteorology and physical oceanography*, **136 (646)**, 30–40.

Jeevanjee, N., D. D. Koll, and N. Lutsko, 2021: "simpson's law" and the spectral cancellation of climate feedbacks. *Geophysical Research Letters*, **48 (14)**, e2021GL093 699.

Lacagnina, C., and F. Selten, 2014: Evaluation of clouds and radiative fluxes in the ec-earth general circulation model. *Climate dynamics*, **43**, 2777–2796.

Loeb, N. G., and Coauthors, 2018: Clouds and the earth's radiant energy system (ceres) energy balanced and filled (ebaf) top-of-atmosphere (toa) edition-4.0 data product. *Journal of climate*, **31 (2)**, 895–918.

Loeb, N. G., and Coauthors, 2022: Evaluating twenty-year trends in earth's energy flows from observations and reanalyses. *Journal of Geophysical Research: Atmospheres*, **127 (12)**, e2022JD036 686.

Madec, G., 2015: Nemo ocean engine, version 3.6 stable note du pole de modelisation de l'institut pierre-simon laplace, vol. 27. *IPSL, Paris: France*.

Martin, G., D. Johnson, and A. Spice, 1994: The measurement and parameterization of effective radius of droplets in warm stratocumulus clouds. *Journal of Atmospheric Sciences*, **51 (13)**, 1823–1842.

Masiello, G., C. Serio, G. Liuzzi, S. Venafra, T. Maestri, M. Martinazzo, U. Amato, and G. Grieco, 2022: sigma-iasi. Zenodo, URL https://doi.org/10.5281/zenodo.7019991, https://doi.org/10.5281/zenodo.7019991.

Masiello, G., C. Serio, T. Maestri, M. Martinazzo, F. Masin, G. Liuzzi, and S. Venafra, 2024: The new σ-iasi code for all sky radiative transfer calculations in the spectral range 10 to 2760 cm-1: σ-iasi/f2n. *Journal of Quantitative Spectroscopy and Radiative Transfer*, **312**, 108 814.

Matricardi, M., 2009: An assessment of the accuracy of the rttov fast radiative transfer model using iasi data. *Atmospheric Chemistry and Physics*, **9 (18)**, 6899–6913.

Meinshausen, M., and Coauthors, 2020: The shared socio-economic pathway (ssp) greenhouse gas concentrations and their extensions to 2500. *Geoscientific Model Development*, **13 (8)**, 3571–3605.

Meyssignac, B., and Coauthors, 2019: Measuring global ocean heat content to estimate the earth energy imbalance. *Frontiers in Marine Science*, **6**, 432.

Mlawer, E. J., S. J. Taubman, P. D. Brown, M. J. Iacono, and S. A. Clough, 1997: Radiative transfer for inhomogeneous atmospheres: Rrtm, a validated correlated-k model for the longwave. *Journal of Geophysical Research: Atmospheres*, **102 (D14)**, 16 663–16 682.

Ou, S.-c., and K.-N. Liou, 1995: Ice microphysics and climatic temperature feedback. *Atmospheric Research*, **35 (2-4)**, 127–138.

Padmanabhan, S., and Coauthors, 2019: The polar radient energy in the far infrared experiment (prefire). *IGARSS 2019-2019 IEEE International Geoscience and Remote Sensing Symposium*, IEEE, 8834–8836.

Palchetti, L., and Coauthors, 2020: unique far-infrared satellite observations to better understand how earth radiates energy to space. *Bulletin of the American meteorological society*, **101 (12)**, E2030–E2046.

Pan, F., X. Huang, S. S. Leroy, P. Lin, L. L. Strow, Y. Ming, and V. Ramaswamy, 2017: The stratospheric changes inferred from 10 years of airs and amsu-a radiances. *Journal of Climate*, **30 (15)**, 6005–6016.

Pan, F., X. Huang, L. L. Strow, and H. Guo, 2015: Linear trends and closures of 10-yr observations of airs stratospheric channels. *Journal of Climate*, **28 (22)**, 8939–8950.

Pincus, R., H. W. Barker, and J.-J. Morcrette, 2003: A fast, flexible, approximate technique for computing radiative transfer in inhomogeneous cloud fields. *Journal of Geophysical Research: Atmospheres*, **108 (D13)**.

Raghuraman, S. P., D. Paynter, and V. Ramaswamy, 2021: Anthropogenic forcing and response yield observed positive trend in earth's energy imbalance. *Nature communications*, **12 (1)**, 4577.

Raghuraman, S. P., D. Paynter, V. Ramaswamy, R. Menzel, and X. Huang, 2023: Greenhouse gas forcing and climate feedback signatures identified in hyperspectral infrared satellite observations. *Geophysical Research Letters*, **50 (24)**, e2023GL103 947.

Räisänen, P., H. W. Barker, M. F. Khairoutdinov, J. Li, and D. A. Randall, 2004: Stochastic generation of subgrid-scale cloudy columns for large-scale models. *Quarterly Journal of the Royal Meteorological Society: A journal of the atmospheric sciences, applied meteorology and physical oceanography*, **130 (601)**, 2047–2067.

Ramaswamy, V., M. Schwarzkopf, W. Randel, B. Santer, B. Soden, and G. Stenchikov, 2006: Anthropogenic and natural influences in the evolution of lower stratospheric cooling. *Science*, **311 (5764)**, 1138–1141.

Ramaswamy, V., and Coauthors, 2001: Stratospheric temperature trends: Observations and model simulations. *Reviews of Geophysics*, **39 (1)**, 71–122.

Roemer, F. E., and S. A. Buehler, 2025: Observations of the clear-sky spectral longwave feedback at surface temperatures between 210 and 310 k. *Journal of Climate*, **38 (11)**, 2589–2604.

Roemer, F. E., S. A. Buehler, M. Brath, L. Kluft, and V. O. John, 2023: Direct observation of earth's spectral long-wave feedback parameter. *Nature Geoscience*, **16 (5)**, 416–421.

Serio, C., G. Masiello, G. Liuzzi, P. Mastro, T. Maestri, M. Martinazzo, F. Masin, and S. Venafra, 2023: Simultaneous retrieval from the full iasi spectrum of cloud and atmospheric parameters using the new all-sky forward model sigma-iasi/f2n: the first day-night infrared retrieval of the antarctica ozone hole. *Remote Sensing of Clouds and the Atmosphere XXVIII*, SPIE, Vol. 12730, 32–43.

Soden, B. J., I. M. Held, R. Colman, K. M. Shell, J. T. Kiehl, and C. A. Shields, 2008: Quantifying climate feedbacks using radiative kernels. *Journal of Climate*, **21 (14)**, 3504–3520.

von Schuckmann, K., and Coauthors, 2020: Heat stored in the earth system: Where does the energy go? the gcos earth heat inventory team. *Earth System Science Data Discussions*, **2020**, 1–45.

Whitburn, S., L. Clarisse, S. Bauduin, M. George, D. Hurtmans, S. Safieddine, P. F. Coheur, and C. Clerbaux, 2020: Spectrally resolved fluxes from iasi data: Retrieval algorithm for clear-sky measurements. *Journal of Climate*, **33 (16)**, 6971–6988.

Whitburn, S., and Coauthors, 2021: Trends in spectrally resolved outgoing longwave radiation from 10 years of satellite measurements. *npj climate and atmospheric science*, **4 (1)**, 48.

Wielicki, B. A., B. R. Barkstrom, E. F. Harrison, R. B. Lee III, G. L. Smith, and J. E. Cooper, 1996: Clouds and the earth's radiant energy system (ceres): An earth observing system experiment. *Bulletin of the American Meteorological Society*, **77 (5)**, 853–868.

Wild, M., 2020: The global energy balance as represented in cmip6 climate models. *Climate Dynamics*, **55 (3)**, 553–577.